ACS Catalysis

Research Article

pubs.acs.org/acscatalysis

Dynamics of CrO_3–Fe_2O_3 Catalysts during the High-Temperature Water-Gas Shift Reaction: Molecular Structures and Reactivity

Christopher J. Keturakis,*[,†,⊥] Minghui Zhu,[†] Emma K. Gibson,[‡,#] Marco Daturi,[‡] Franklin Tao,[§] Anatoly I. Frenkel,[∥] and Israel E. Wachs*[,†]

[†]Operando Molecular Spectroscopy and Catalysis Laboratory, Chemical Engineering Department, Lehigh University, Bethlehem, Pennsylvania 18015, United States

[‡]Laboratoire Catalyse et Spectrochimie, ENSICAEN, Université de Caen, CNRS, 6 Bd Maréchal Juin, F-14050 Caen Cedex, France

[§]Department of Chemical & Petroleum Engineering, University of Kansas, Lawrence, Kansas 66047, United States

[∥]Department of Physics, Yeshiva University, New York, New York 10016, United States

Supporting Information

ABSTRACT: A series of supported CrO_3/Fe_2O_3 catalysts were investigated for the high-temperature water-gas shift (WGS) and reverse-WGS reactions and extensively characterized using in situ and operando IR, Raman, and XAS spectroscopy during the high-temperature WGS/RWGS reactions. The in situ spectroscopy examinations reveal that the initial oxidized catalysts contain surface dioxo $(O{=})_2Cr^{6+}O_2$ species and a bulk Fe_2O_3 phase containing some Cr^{3+} substituted into the iron oxide bulk lattice. Operando spectroscopy studies during the high-temperature WGS/RWGS reactions show that the catalyst transforms during the reaction. The crystalline Fe_2O_3 bulk phase becomes Fe_3O_4 ,and surface dioxo $(O{=})_2Cr^{6+}O_2$ species are reduced and mostly dissolve into the iron oxide bulk lattice. Consequently, the chromium–iron oxide catalyst surface is dominated by FeO_x sites, but some minor reduced surface chromia sites are also retained. The $Fe_{3-x}Cr_xO_4$ solid solution stabilizes the iron oxide phase from reducing to metallic Fe^0 and imparts an enhanced surface area to the catalyst. Isotopic exchange studies with $C^{16}O_2/H_2 \rightarrow C^{18}O_2/H_2$ isotopic switch directly show that the RWGS reaction proceeds via the redox mechanism and only O* sites from the surface region of the chromium–iron oxide catalysts are involved in the RWGS reaction. The number of redox O* sites was quantitatively determined with the isotope exchange measurements under appropriate WGS conditions and demonstrated that previous methods have undercounted the number of sites by nearly 1 order of magnitude. The TOF values suggest that only the redox O* sites affiliated with iron oxide are catalytic active sites for WGS/RWGS, though a carbonate oxygen exchange mechanism was demonstrated to exist, and that chromia is only a textural promoter that increases the number of catalytic active sites without any chemical promotion effect.

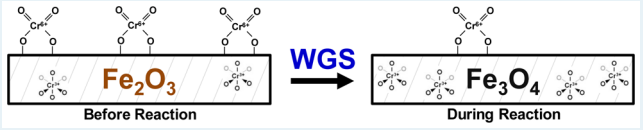

KEYWORDS: *water–gas shift, operando, in situ, spectroscopy, metal oxide, isotope exchange, surface*

1. INTRODUCTION

Mixtures of carbon monoxide and hydrogen, "syngas" or "water gas", are encountered in many crucial industrial processes, including the manufacturing of ammonia (Haber–Bosch process), methanol, hydrogen (steam methane reforming (SMR), water-gas shift (WGS)), and hydrocarbons (Fischer–Tropsch (FT)).[1−4] Water gas was used as a source of hydrogen for the Haber–Bosch process by converting H_2O to H_2 and CO to CO_2, since CO was a catalyst poison and needed to be removed from the water-gas stream. In 1914, Bosch and Wild implemented an iron–chromium oxide catalyst that converted CO into CO_2, an easily separable chemical, at 400–500 °C.[5] This first popularized the use of the WGS reaction (eq 1), though the reaction was discovered more than a century earlier. Nearly the same iron–chromium oxide based catalyst is still used today industrially, but with the addition of small amounts of copper.

$$H_2O + CO \leftrightarrow H_2 + CO_2 \quad (1)$$

Catalysts for the WGS reaction are divided into several groups. Iron and chromium oxide based catalysts are used for the high-temperature WGS (HTS) at 350–450 °C, and copper–zinc–aluminum oxide based catalysts are used for the low-temperature WGS (LTS) at 190–250 °C. Additionally, there has been research into medium-temperature shift (MTS) catalysts and sulfur-tolerant "sour gas" shift catalysts. There have been many recent advancements in our understanding of the LTS catalysts,[2,6] but HTS catalysts remain poorly understood and nearly unchanged in composition for industrial use. The water-gas shift reaction has been studied for over a century, and several good reviews of the literature already exist. Newsome reviewed the catalysis literature up to 1980,[4] Rhodes et al. reviewed the literature up to 1995,[1] Ladebeck and Wagner provided a review up to 2003 with an emphasis on fuel cell

Received: May 7, 2016
Revised: June 6, 2016

DOI: 10.1021/acscatal.6b01281
ACS Catal. 2016, 6, 4786–4798

applications,[7] Ratnasamy and Wagner reviewed recent developments up to 2009,[2] and Zhu and Wachs focused on iron-based catalyst research up to 2016.[8] In recent years, there has also been an interest in developing Cr-free iron oxide based HTS catalysts because of the toxicity of hexavalent chromium, but successful substitutes have still not been achieved.[9] This literature review will primarily focus on new characterization studies performed in the last two decades that provide new insights to the HTS chromium−iron oxide catalysts but will also explore older, relevant publications if they contain additional insights.

1.1. Ambient and ex Situ Characterization. It is well-known that ambient and ex situ or postreaction characterization suffers from some fundamental problems, such as sample hydration, oxidation, and hydrocarbon adsorption, which limit the usefulness of such data. It is now also well established that catalyst surfaces are dynamic under reaction conditions, a trait that cannot be fully appreciated and understood without in situ and operando spectroscopy analysis.[10] Ambient and ex situ characterizations of the iron−chromium oxide HTS catalyst have been performed with many techniques, including X-ray diffraction (XRD), IR spectroscopy, electron microscopy, X-ray absorption spectroscopy (XAS), X-ray photoelectron spectroscopy (XPS), and Mössbauer spectroscopy.[11−35] The results of these studies have reached the following conclusions: (1) the fresh catalyst is a Fe_2O_3 phase, typically either α or γ depending on synthesis and calcination conditions, (2) both Cr^{3+} and Cr^{6+} exist in the fresh catalyst, (3) Cr^{3+} is substituted preferentially into the iron oxide lattice octahedral sites (O_h) but not tetrahedral sites (T_d), (4) there is some surface segregation of chromium, (5) the reduced catalyst contains Fe_3O_4 (magnetite), and (6) discrete Cr_2O_3 particles are present above ∼14 wt % Cr_2O_3/Fe_2O_3.

1.2. In Situ and Operando Spectroscopy Characterization. There have been extensive studies on iron oxides, especially in situ IR studies, due to the additional interest from the Fischer−Tropsch community.[36−47] Boudjemaa et al. performed in situ IR spectroscopy on unpromoted Fe_2O_3 during the WGS at 450 °C[47] and did not detect any surface reaction intermediates at this high temperature. Relevant surface intermediates such as formates and carbonates, however, are not expected to exist at this high temperature.[36−42] Busca and Lorenzelli examined the IR spectrum of a dehydrated $FeCrO_3$ catalyst and noted that a Cr^{6+}═O band is present but could not identify its origin.[48] In situ Mössbauer spectroscopy of iron oxide catalysts under gas mixtures with different oxyreduction potentials revealed that nonstoichiometric Fe_3O_4 was formed and that the stoichiometry depended on the oxyreduction potential of the gas mixture.[49,50] Furthermore, the oxygen vacancy in the iron oxide was found to correlate with catalyst activity up to 350 °C. In situ XRD measurements by Zanchet et al. confirmed the transformation of Fe_2O_3 to Fe_3O_4 during the HTS at 350 °C and above.[51] Kendelewicz et al. performed in situ ambient-pressure XPS (AP-XPS) studies of room-temperature water adsorption (partial pressures of 10^{-9} to 2 Torr) on Fe_3O_4 and combined the results with density functional theory (DFT) calculations.[52] It was found that at lower partial pressures, $\leq 10^{-4}-10^{-5}$ Torr, water does not dissociatively adsorb on the surface, except on defect sites, and progressive dissociation into surface hydroxyl species takes place between 10^{-4} and 10^{-2} Torr.

Only one operando spectroscopy characterization experiment has been performed on the HTS catalysts of iron oxide and chromium−iron oxides. A rather unique study by Patlolla et al. combines three spectroscopic techniques (XAS, XRD, and Raman spectroscopy) with simultaneous online mass spectrometry (MS) for product analysis.[53] The quality of the Raman spectroscopy probe was insufficient for collection of data at high temperatures, thus only allowing the Raman data to be collected in situ before the HTS reaction and at room temperature ex situ after cooling in the WGS mixture. In situ Raman spectroscopy indicated the presence of hydrated CrO_4^{2-} oxoanions before the reaction and demonstrated their disappearance, interpreted as reduction, after reaction. Before reaction, both catalysts were a mixture of γ-/α-Fe_2O_3 at elevated temperatures and only γ-Fe_2O_3 was present after cooling to room temperature. The corresponding operando XRD measurements confirmed that the catalysts were γ-Fe_2O_3 before the reaction, Fe_3O_4 during the reaction, and returned to γ-Fe_2O_3 upon cooling to room temperature. The operando XAS Fe K edge data demonstrated that the catalysts were in the Fe^{3+} oxidation state before the reaction and were partially reduced during the HTS reaction, which is consistent with Fe_3O_4 formation.

1.3. Catalytic Active Site and Reaction Mechanism. Research concerning the nature and strength of oxygen bonds of metal oxides and their correlation to catalytic activity has been a topic of interest for many decades.[54−60] The adsorption and relaxation kinetics of CO/CO_2 and H_2/H_2O gas mixtures indicated that surface oxygen sites and vacancies were the adsorption sites for the WGS reactants and products and comprised ∼10−20% of the BET surface area under the conditions studied (pressures <40 kPa or ∼0.4 atm and temperatures of ∼340−400 °C).[12,57,58,61−65]

Recently, the idea of counting sites was revisited by Zhu and Wachs, who used the $C^{16}O_2/H_2 \Leftrightarrow C^{18}O_2/H_2$ isotope exchange to count the number of participating oxygen sites during the reaction under more industrially relevant conditions (pressures of 1 atm and temperatures of ∼330−400 °C) followed by postisotope exchange H_2-TPR to probe the total amount of exchanged oxygen. Their results indicated that the entire surface layer of the catalyst is participating in the reaction and that previous oxygen site counting methods were significantly undercounting the number of participating sites by almost 1 order of magnitude and, consequently, reporting turnover frequencies 1 order of magnitude or greater.[66]

The reaction mechanism has been debated for many decades with kinetic equations based on a regenerative or associative mechanism having some quantitative differences, albeit small differences, from the overall reaction kinetics.[2,4,12,58,61,67] Furthermore, experimental proof exists for both mechanisms. Equilibrium and kinetic measurements of individual reactants/products or with CO_2/CO and H_2O/H_2 gas mixtures has indicated that the regenerative mechanism is the primary pathway for the HT-WGS reaction.[12,55,57,61,62,64,65,67−69] Many of these same experiments, however, suggest that a second pathway may also exist due to the discrepancies between model and experimental rates mentioned above.[12,57,61,70] Research has suggested both surface formate and carbonate species, with experimental evidence for carbonates coming from isotope exchanges.[57,70−76]

Paradigm shifts in the fundamental understanding of heterogeneous catalysts have occurred since research on the chromium−iron oxide catalyst began over a century ago, and it is now accepted that catalysts are dynamic during the reaction and heterogeneous catalytic reactions only take place on the

DOI: 10.1021/acscatal.6b01281
ACS Catal. 2016, 6, 4786−4798

surface of solid catalysts. The absence of extensive fundamental in situ and operando spectroscopic studies of the surface of the Cr_2O_3/Fe_2O_3 catalyst under appropriate HT-WGS conditions in the catalysis literature has hindered the development of molecular level insights about the catalytic active sites, surface reaction intermediates, and reaction mechanism. To address the surface properties of chromia−iron oxide catalysts during HT-WGS, a series of supported CrO_3/Fe_2O_3 catalysts were prepared and extensively characterized using operando Raman, IR, XAS, and in situ AP-XPS spectroscopy. Potential surface reaction intermediates were examined with in situ IR spectroscopy during adsorption of probe molecules (CO, CO_2, HCOOH, and CH_3OH) and also monitored during the WGS reaction with operando IR spectroscopy. The redox characteristics of the chromium−iron oxide catalysts were determined by redox studies during in situ Raman and operando IR spectroscopy. The new fundamental insights allow the development of structure−reactivity relationships for the high-temperature WGS by supported CrO_3/Fe_2O_3 catalysts under realistic WGS conditions.

2. EXPERIMENTAL SECTION

2.1. Catalyst Synthesis and Preparation. The supported CrO_3/Fe_2O_3 catalysts were prepared by incipient wetness impregnation of aqueous solutions of chromium(III) nitrate ($Cr(NO_3)_3{\cdot}9H_2O$, Alfa Aesar, 98.5%) and distilled water on an iron oxide support (γ-Fe_2O_3, Alfa Aesar, 99+%), using an incipient wetness point of ∼0.4 mL/g of Fe_2O_3 under ambient conditions. Samples were prepared with chromium oxide loadings of 1, 2, 3, 5, 7, and 9 wt % CrO_3. The samples were dried overnight under ambient conditions, followed by a second drying step on exposure to ambient air at 100 °C for 4 h in a programmable furnace (Thermolyne, Model 48000). Finally, the samples were subjected to calcination by ramping the temperature at 5 °C/min under flowing air (Airgas, Zero grade) to 350 °C for 2 h. The final synthesized catalysts are denoted as *x*% CrO_3/Fe_2O_3, where *x* is the weight percent of chromium oxide.

2.2. BET Specific Surface Area. The BET surface area of the catalyst samples was measured by nitrogen adsorption−desorption in flowing N_2 at −196 °C with a Quantasorb surface area analyzer (Quantachrome Corp., Model OS-9). A sample quantity of ∼0.3 g was typically employed for the measurement, and the sample was outgassed at 250 °C before N_2 adsorption (Quantachrome Corp., Model QT-3).

2.3. In Situ FTIR Spectroscopy and Probe Molecules/Reactions. All FTIR studies on supported catalysts in section 2.3 were performed at the University of Caen, Caen, France. For FTIR spectroscopy studies, the powdered catalyst samples were pressed into disks of ∼10 mg/cm^2 and activated in situ in the IR quartz cell equipped with KBr windows and attached to a high-vacuum system.[77] Activation consisted of heating the catalyst at a rate of 10 °C/min under 13 kPa of O_2 from room temperature to 350 °C. The sample was held at 350 °C for 45−60 min followed by cell evacuation at the same temperature for 30 min. The sample disk was moved from the furnace part of the cell to the optical section. Spectra were recorded at room temperature with a Nicolet Magna 550 FTIR spectrometer using 4 cm^{-1} resolution and 128 scans. They were treated by the Nicolet OMNIC software. For the mixed-metal oxide catalysts, diffuse reflectance FTIR (DRIFTS) was performed at Lehigh University in a Thermo Nicolet 8700 spectrometer equipped with a commercial Harrick high-temperature reaction chamber and praying mantis DRIFTS mirrors. The standard activation procedure is described in section 2.4.

2.3.1. Carbon Monoxide and Carbon Dioxide Probe Molecules. After catalyst activation under oxidizing conditions (10% O_2/Ar (Airgas, certified, 10.00% O_2/Ar balance)), liquid nitrogen was added to a jacket surrounding the reaction cell, except for optical windows, in order to cool the sample to −196 °C (100 K). For CO_2 adsorption, the jacket was, instead, filled with solid CO_2 to reach −78 °C (195 K). A glass bulb containing CO or CO_2 gas was attached to the vacuum system and incrementally dosed on the basis of pressure gauges and a calibrated volume. The gas was introduced so that the total partial pressure of CO or CO_2 in the cell was increased incrementally from 1 to 100 Torr, with an IR spectrum taken at each increment. After 100 Torr was reached, an equilibrium partial pressure of CO or CO_2 between the glass bulb and cell was achieved, followed by the collection of another IR spectrum. After CO or CO_2 equilibration, the cell was evacuated to see if any species remained on the surface. If species remained on the surface of the catalyst, then the temperature was increased, first to room temperature by allowing the liquid nitrogen or solid CO_2 to evaporate and then at 10 °C/min until the surface species desorbed. Spectra were collected every 25 or 50 °C.

2.3.2. Formic Acid and Methanol Probe Molecules. After catalyst activation under oxidizing conditions (10% O_2/Ar (Airgas, certified, 10.00% O_2/Ar balance)), a glass bulb containing HCOOH or CH_3OH was attached to the vacuum system and incrementally dosed on the basis of pressure gauges. The gas was introduced so that the total partial pressure of HCOOH or CH_3OH in the cell was increased incrementally from 1 to 100 Torr, with an IR spectrum taken at each increment. After 100 Torr was reached, an equilibrium partial pressure of HCOOH or CH_3OH was allowed into the cell, followed by the collection of another IR spectrum. After HCOOH or CH_3OH equilibration, the cell was evacuated to eliminate any physisorbed species on the surface. The catalyst temperature was ramped at 10 °C/min until the chemisorbed species desorbed. Spectra were collected every 25 or 50 °C.

2.4. In Situ Raman Spectroscopy. The Raman spectra of the chromiun−iron oxide catalysts were obtained with a high-resolution, dispersive Raman spectrometer system (Horiba-Jobin Yvon LabRam HR) equipped with three laser excitations (532, 442, and 325 nm). The visible laser at 442 nm (violet) and the UV laser at 325 nm (not visible) were generated by a He−Cd laser (Kimmon, Model No. IK5751I-G). The lasers were focused on the samples with a confocal microscope equipped with a 50× long working distance objective (Olympus BX-30- LWD) for the visible lasers and 15× objective (OFR LMU- 15X-NUV) for the UV laser. The LabRam HR spectrometer was optimized for the best spectral resolution by employing a 900 groove/mm grating (Horiba-Jobin Yvon 51093140HR) for the visible lasers and a 2400 groove/mm grating (Horiba-Jobin Yvon HR) for the UV laser. The resolution for both gratings is ∼1 cm^{-1}. The Rayleigh scattered light was rejected with holographic notch filters (Kaiser Super Notch). The notch filter window cutoffs were ∼100 and ∼300 cm^{-1} with the visible lasers and UV laser, respectively. The scattered light, after the Rayleigh scattering was removed, was directed into a UV-sensitive liquid N_2 cooled CCD detector (Horiba-Jobin Yvon CCD-3000 V). The calibration of each laser line was performed with an Hg lamp by adjusting the groove gratings to match the zero position and minimize the

DOI: 10.1021/acscatal.6b01281
ACS Catal. 2016, 6, 4786−4798

error of the linearity across the full Raman spectrum range. The Hg lines chosen to represent the 532, 442, and 325 nm lasers were 546.07, 441.6, and 365.02 nm, respectively. Additionally, wavenumber calibration of the Raman spectrograph was checked using the silicon line at 520.7 cm^{-1}.

The catalyst samples, typically consisting of between 5 and 10 mg of loose powder, were placed in an environmentally controlled high-temperature cell reactor (Harrick high-temperature reaction chamber) containing a quartz window and O-ring seals that were cooled with flowing cooling water. The sample temperature was controlled by a temperature controller (Harrick ATC/low voltage temperature control unit), providing linear heating rates of over 50 °C/min through a K-type thermocouple. The catalyst bed, however, was fitted with a second K-type thermocouple for cascade control. Typical reactor cell conditions were room temperature to 400 °C, 10−20 °C/min heating and cooling rates, atmospheric pressure, and ∼40 sccm gas flow rates metered by mass flow controllers (Brooks, Model 5850E series).

The protocol for obtaining in situ Raman spectra under an oxidizing (O_2/Ar) environment was as follows. The sample was initially heated at a rate of 10 °C/min in the in situ cell to 350 °C and held for 45−60 min under flowing 10% O_2/Ar (Airgas, certified, 10.00% O_2/Ar balance). For the acquisition of the Raman spectra, only the laser angles parallel to the incident beam were allowed to hit the catalyst sample, where the accumulation was collected at 10 s/scan for seven scans with a 200 μm hole. The Raman spectra were collected with the 442 nm laser, due to known CrO_x resonance enhancement,[78] at 350 °C and also at room temperature after dehydration under the oxidizing conditions.

2.5. Operando Raman Spectroscopy and in Situ Redox Cycles. The reverse-WGS (RWGS) was performed using the same Harrick high-temperature reaction chamber, and all Raman spectra were collected with a 442 nm laser. The gaseous outlet from the flow-through fixed-bed reactor was heated to 120 °C and connected to an online mass spectrometer (Varian, 1200L quadrupole). The online MS spectra were collected every 0.5 s and m/e values of 15−75 simultaneously monitored. The m/z values used to detect the reactants and products were m/z 28 (CO), m/z 44 (CO_2), and m/z 18 (H_2O), with the CO signal corrected for CO_2 cracking in the MS. The Raman spectra were collected under reaction conditions with the simultaneous MS analysis of the reaction product stream to constitute the operando spectroscopy experimental mode.

The catalysts underwent the same dehydration procedure as described in section 2.3. After dehydration, the catalysts were heated to 400 °C at 10 °C/min, still under the O_2/Ar environment. At 400 °C and after a short inert flush (15 min), a reverse-WGS feed of X% H_2/Y% CO_2/Ar flowing at 42 cm^3/min total was introduced into the reactor cell. Experiments were repeated with the same total flow rate but with H_2:CO_2 ratios ranging from 0.5 to 4. Spectra accumulation consisted of 120 s/scan for five scans. Spectra were collected every 5 min for the first 10 min and then once every subsequent 20 min. The samples were run for a minimum of 60 min.

To determine the redox capabilities of the samples, the catalysts were allowed to reach steady state during RWGS (typically 60−120 min) before an inert flush was performed for 5 min at 400 °C. After the flush, a mixture of either 33% CO_2/He or 2.5% H_2O/He (bubbled) was sent through the reactor for 30 min. Another inert flush was performed for 5 min before finally introducing a 10% O_2/Ar gas mixture into the reactor at 400 °C for another 60 min to perform the final reoxidation. Raman spectra were collected after each step.

2.6. Operando X-ray Absorption Spectroscopy (XAS). The X-ray absorption spectroscopy (XAS) experiments were performed at Brookhaven National Laboratory (BNL) National Synchrotron Light Source (NSLS) beamline X19A. The Cr and Fe K-edge XAS data were obtained in fluorescence mode, using a PIPS detector. The monochromator Si(111) crystals were detuned 30% to minimize harmonics. The powder samples were loaded in a 1.0 mm o.d. (0.9 mm i.d.) quartz capillary, known also as a Clausen cell. An Omega thermocouple was inserted into the capillary and placed adjacent to and in contact with the catalyst bed. The catalyst sample was heated by using a resistive heater placed under the catalyst bed. The temperature was controlled using an Eurotherm temperature controller, and gas flow into the cell was controlled by Brooks mass flow controllers. The catalyst was activated by flowing 10% O_2/He at 30 cm^3/min flow rate and ramping the temperature to 350 °C at a 10 °C/min heating rate, followed by annealing at 350 °C for 45−60 min. For the WGS reaction, the temperature was raised to 400 °C and the WGS reaction mixture introduced into the cell by directing CO mixed with helium through a water bubbler before entering the reactor (resulting in ∼3% H_2O and a H_2O:CO ratio of 2:1). The data were then collected at 400 °C during the WGS reaction mixture flow. Simultaneous online product analysis was done using a 0−100 amu quadrupole mass spectrometer (SRS). The WGS reaction was performed for ∼90 min or until the reaction appeared to reach steady-state conversion. After the reaction, the catalyst was typically cooled to 350 °C under flowing 10% O_2/He and held for ∼30 min before cooling to room temperature under the same atmosphere. Data were collected at 350 °C and at room temperature. The Fe K-edge EXAFS data were corrected for self-absorption by comparing the data measured in the Clausen cell under ambient conditions and using tape samples measured in transmission mode that were free from self-absorption distortion. This comparison allowed us to obtain the scaling factor that was later applied to all operando XAS spectra to correct for self-absorption effects.[79]

2.7. In Situ Ambient-Pressure X-ray Photoelectron Spectroscopy (AP-XPS). AP-XPS studies were performed by the group of F.T. by using a laboratory-based ambient-pressure X-ray photoelectron spectrometer.[80−82] An Al Kα monochromator (Microfocus 600) made by Specs Surface Nano Analysis GmbH was used as the X-ray source. The energy analyzer was a Phobios 150 instrument. The sample was introduced into the reaction cell of this system. The CO and water vapor were mixed before introduction to the reaction cell. The introduction of H_2O (1 Torr) and CO (0.5 Torr) was confirmed with a mass spectrometer installed on lens 1. Photoemission features of Fe 2p and Cr 2p were collected during the WGS reaction as a function of temperature. Catalytic activity was confirmed by formation of H_2 and CO_2 reaction products with the online mass spectrometer.

2.8. $C^{16}O_2$/$C^{18}O_2$ Isotope Exchange during RWGS. The $C^{16}O_2$/$C^{18}O_2$ isotope exchange experiments were carried out in an Altamira Instruments system (AMI 200) reactor connected to a Dymaxion Dycor mass spectrometer (DME200MS). About 20 mg of catalyst was loaded into a quartz U tube and was dehydrated with 10% O_2/Ar at 400 °C. After dehydration, the iron−chromium oxide catalyst was first allowed to equilibrate under $C^{16}O_2$/H_2 reverse-WGS reaction conditions (10 mL/

DOI: 10.1021/acscatal.6b01281
ACS Catal. 2016, 6, 4786−4798

min $C^{16}O_2$, 10 mL/min H_2) at 330 °C for 1 h and then the catalyst was flushed by inert gas (20 mL/min He) for 10 min followed by a switch to isotopic reverse-WGS reaction conditions (10 mL/min $C^{18}O_2$, 10 mL/min H_2). The $C^{16}O_2$/$C^{18}O_2$ isotope exchange was monitored with the online mass spectrometer by recording the evolution of $H_2{}^{16}O$, $H_2{}^{18}O$, $C^{16}O_2$, $C^{16}O^{18}O$, and $C^{18}O_2$ species (m/z 17, 19, 44, 46, 48). All MS signals were normalized to the same maximum and minimum intensity to observe their transient behavior.

3. RESULTS

3.1. Characterization before WGS/RWGS Reactions. A suite of in situ spectroscopy techniques, IR, Raman, XANES, and XPS, were used to characterize the molecular structure of the supported CrO_3/Fe_2O_3 catalyst before the reaction. In all experiments, the catalyst was pretreated at 350 °C in an oxidizing environment, which is considered to be the "before" reaction state. All techniques (section S2.1 and Figures S1−S4 in the Supporting Information) indicate that the initial iron oxide phase is Fe_2O_3 (Raman, γ-Fe_2O_3 bands present; IR, Fe_2O_3 bands present; XANES, Fe K-edge spectra match Fe_2O_3 reference compound; XPS, Fe 2p region exhibits characteristic peaks, shoulders, and satellite peaks of Fe^{3+} from Fe_2O_3). Additionally, in situ IR spectra (Figure S1) revealed strong bands at 1008 cm^{-1} along with a shoulder at 993 cm^{-1}. The corresponding in situ Raman spectroscopy (Figure S2) exhibits a band at 997 cm^{-1}. The band at ∼1008 cm^{-1} is assigned to $\nu_{as}(Cr(=O)_2)$, and the band at ∼993−997 cm^{-1} is assigned to $\nu_s(Cr(=O)_2)$ vibrations of a surface dioxo $(O=)_2CrO_2$ species.[78,83−85] The Cr-free Fe_2O_3 sample exhibits many surface hydroxyl vibrations, and the titration of these hydroxyls with increasing chromia loading reveals that the surface $(O=)_2CrO_2$ species anchor by reacting with surface Fe−OH species. The surface hydroxyl titration suggests that ∼3% CrO_3/Fe_2O_3 is the surface CrO_x monolayer coverage, but the reappearance of some surface hydroxyls upon further addition of chromia above monolayer coverage suggests that the iron oxide surface is re-exposed (either from clustering of chromia on the surface or its dissolution into the bulk). The in situ Raman spectrum (Figure S2) also possesses a band at 842 cm^{-1} from the ν(Cr−O−Fe) bridging bond between the surface dioxo species and Fe_2O_3 support.[78] A small, unlabeled band at 571 cm^{-1} is present for the 9% CrO_3/Fe_2O_3 catalyst and may indicate the presence of a minor amount of Cr_2O_3 nanoparticles (expected sharp band at 550 cm^{-1}).[78] In situ XANES Cr K-edge spectra (Figure S3) reveal that the monolayer catalyst (3% CrO_3/Fe_2O_3) almost exclusively possesses $Cr^{6+}O_4$ from the intense XANES pre-edge peak, while the 9% CrO_3/Fe_2O_3 catalyst possesses a mixture of $Cr^{6+}O_4$ and $Cr^{3+}O_6$ on the basis of reference compounds (see Figure S5 in the Supporting Information for reference compounds). The Cr 2p region of the in situ XPS spectra (Figure S4) exhibits a peak at ∼578.7 ± 0.2 eV from Cr^{6+} $2p_{3/2}$ electrons[86−91] and two major Cr^{3+} $2p_{3/2}$ peaks at 576.6 and 575.6 eV similar to that of Cr_2O_3.[87] All in situ spectra and a detailed analysis of each band/peak are given in section S2.1 and Figures S1−S4.

3.2. Probe Molecules and Reactions. *3.2.1. In Situ IR for Adsorption of CO_2, CO, and HCOOH.* Adsorption of the WGS reactants/products CO_2 and CO was investigated at low temperatures in an IR spectroscopy system, while adsorption of formic acid (HCOOH) was investigated at elevated temperatures, and the results are given in Figures S6−S8 in the Supporting Information, respectively. The adsorption of CO_2 on the Fe_2O_3 support (Figure S6) initially exhibits bands characteristic of carboxylates, bicarbonates, bidentate carbonates, and bridged carbonates, but as the catalyst is warmed to room temperature bands from a minor amount of surface formates (HCOO*) appear. The supported 3% CrO_3/Fe_2O_3 catalyst does not exhibit any major bands from carbonates, and as the catalyst is warmed strong bands from surface formates appear which interact with surface dioxo $(O=)_2CrO_2$ species. The IR spectra for carbon monoxide adsorption are presented in Figure S7 and reveal that CO primarily bonds weakly with surface hydroxyls, indicating the presence of weak Brønsted sites (slightly more acidic than on silica).[93,94] Additionally, a small amount of CO reactively adsorbs, forming carboxylate and carbonate species, as seen for CO_2 adsorption, but the coordination of each is unknown due to poor definition of the IR bands. Corresponding in situ IR spectra for CO_2 and CO adsorption on the bulk Cr_2O_3*Fe_2O_3 mixed-metal oxide catalysts were not undertaken.

Given that surface formate is the most proposed surface reaction intermediate during the WGS reaction,[1,2,4] in situ adsorption of HCOOH was investigated in a temperature-programmed IR spectroscopy system to determine the coordination and thermal stability of surface formate species and the spectra are shown in Figure S8 in the Supporting Information (difference spectra). The Fe_2O_3 catalyst exhibits several adsorbed species at 100 °C: physisorbed HCOOH, two bidentate formates (bidentate-I and -II), and a monodentate formate with bands summarized in Table S1 in the Supporting Information.[38,95−98] All surface formates decompose by 250 °C. The supported 3% CrO_3/Fe_2O_3 (monolayer coverage) catalyst exhibits only one major surface bidentate formate species and a minor amount of surface monodentate formate. The bidentate formate is thermally stable on the catalyst surface until 325 °C, while the monodentate formate desorbs by 250 °C. The supported 9% CrO_3/Fe_2O_3 catalyst exhibits some bands from all four formates observed on the Fe_2O_3 catalyst. The bidentate-I and -II formates decompose by 300 °C, while the monodentate formate decomposes by 250 °C. The negative band at 1008−1014 cm^{-1} on all Cr-containing catalysts indicates that adsorbed formates interact with the surface $(O=)_2CrO_2$ species. Catalysts containing the Cr oxide promoter exhibited higher thermal stability of surface formates in comparison to pure Fe_2O_3 and also preferred a bidentate formate coordination, which is the major species for the monolayer catalyst.

3.3. Characterization during and after the WGS/RWGS Reactions. *3.3.1. BET Surface Area.* The BET surface areas of the freshly calcined and used catalysts are indicated in Table 1. The addition of chromia to the catalysts only slightly decreases the initial surface area before the reaction from ∼88 to 82−84 m^2/g. After the RWGS reaction, the surface area of the catalysts dramatically decreases. While the surface area of the Cr-free Fe_2O_3 catalyst decreases by 1 order of magnitude, the addition

Table 1. BET Surface Areas of the Supported CrO_3/Fe_2O_3 Catalysts before and after the Reverse-WGS (RWGS) Reaction

catalyst	before RWGS (m^2/g)	after RWGS (m^2/g)
Fe_2O_3	88.2	8.4
3% CrO_3/Fe_2O_3	81.5	11
9% CrO_3/Fe_2O_3	83.9	20.5

DOI: 10.1021/acscatal.6b01281
ACS Catal. 2016, 6, 4786−4798

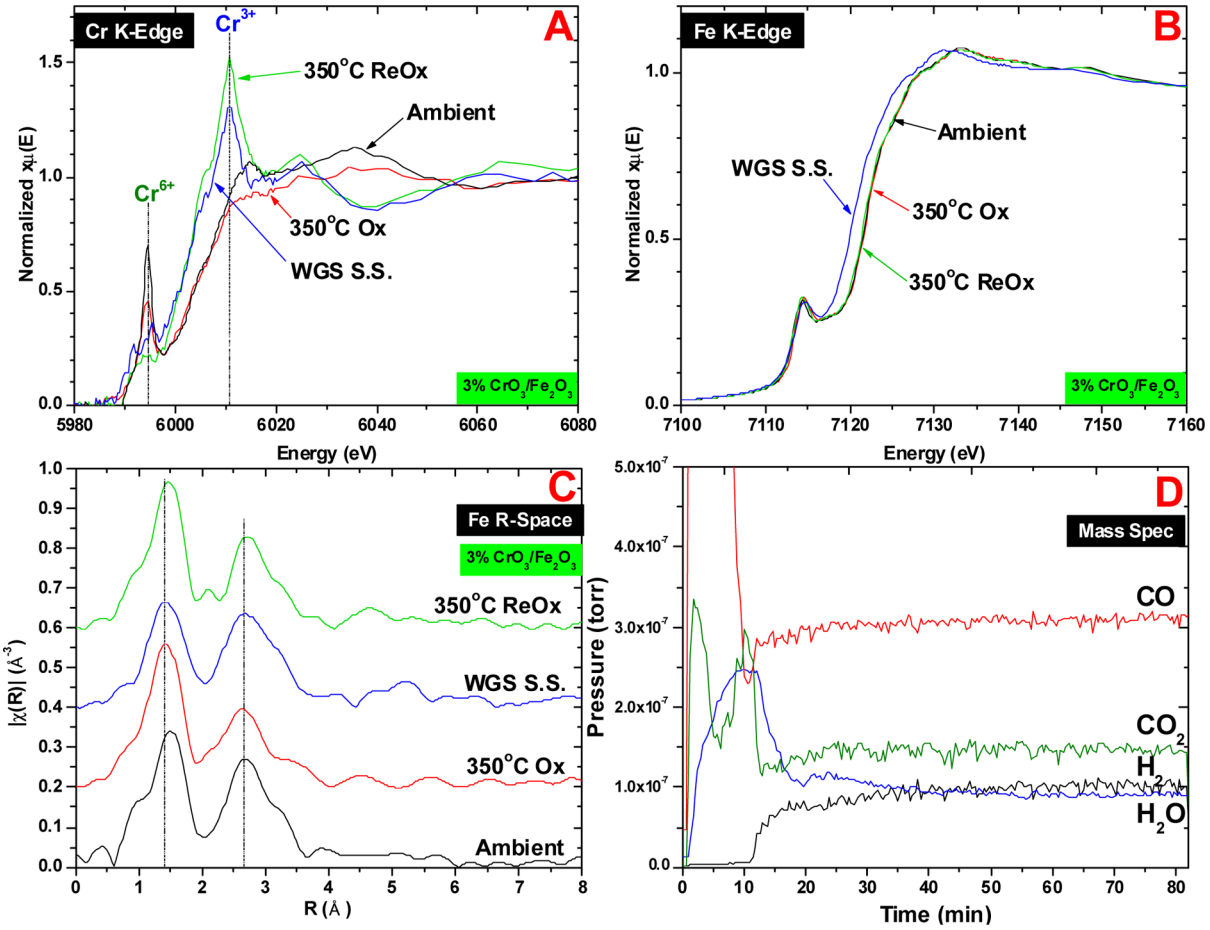

Figure 1. Operando XANES/EXAFS spectra of 3% CrO_3/Fe_2O_3 at room temperature (ambient), before WGS (350 °C Ox), during WGS at 400 °C (WGS S.S.), and reoxidized after WGS (350 °C ReOx): (A) XANES Cr K-edge spectra; (B) XANES Fe K-edge spectra; (C) EXAFS Fe *R*-space spectra; (D) RGA data.

of chromia to iron oxide stabilizes the surface area of the supported CrO_3/Fe_2O_3 catalysts (factors of 1.36× and 2.44× for 3% and 9% CrO_3/Fe_2O_3, respectively).

3.3.2. Operando Raman Spectroscopy. To investigate the phase changes of the catalysts during reaction, Raman spectroscopy measurements were performed at 400 °C with simultaneous gas-phase monitoring using an online MS (operando spectroscopy methodology). The results during the RWGS with H_2:CO_2 ratios ranging from 0.5 to 4 are presented in Figures S9−S11 in the Supporting Information for Fe_2O_3, 3% CrO_3/Fe_2O_3, and 9% CrO_3/Fe_2O_3 catalysts, respectively. The operando Raman spectra of the Fe_2O_3 catalyst (Figure S9) indicate that the catalyst transitions from a Fe_2O_3 phase to Fe_3O_4 during the reaction, at all H_2:CO_2 ratios tested, while the corresponding MS signal shows steady-state production of CO and H_2O after 60 min, confirming the equilibrated state of the catalyst. The operando Raman spectra of the supported 3% and 9% CrO_3/Fe_2O_3 catalysts are shown in Figures S10 and S11 and indicate the same bulk iron oxide transformation. Furthermore, Raman bands for the surface $(O{=})_2CrO_2$ species are initially present at 835 (ν(Cr−O−Fe)) and 996 cm^{-1} (ν_s(Cr(=O)$_2$)) but disappear during the RWGS reaction, suggesting that the surface chromia sites have altered and most likely became reduced. The same results are also observed for all examined H_2:CO_2 ratios. These findings reveal that Fe_3O_4 is also the main bulk iron oxide phase present for all chromium−iron oxide catalysts during the RWGS reaction. A more detailed analysis of the data is given in the section S2.3 in the Supporting Information.

3.3.3. Operando X-ray Absorption Spectroscopy (XAS). The dynamics of the Fe and Cr bonding environments (Fe−X and Cr−X) and oxidation states during the WGS reaction were probed by XAS studies at 400 °C (labeled WGS S.S.) with simultaneous monitoring of the gas phase using a RGA mass spectrometer (operando spectroscopy methodology). The spectral results during WGS (H_2O:CO = 2) for Fe_2O_3 (Figure S12 in the Supporting Information), supported 3% CrO_3/Fe_2O_3 (Figure 1), and supported 9% CrO_3/Fe_2O_3 (Figure S13 in the Supporting Information) are presented in the respective figures.

The Fe K-edge XANES spectra of iron oxide before, during, and after the WGS reaction are presented in Figure S12A in the Supporting Information. The XANES spectrum before the reaction (ambient and 350 °C Ox) is consistent with the Fe_2O_3 bulk phase (α, γ, or their mixture) from the pre-edge feature and edge position (reference compounds given in Figure S14 in the Supporting Information).[92,99] After ∼70 min of the WGS reaction (WGS S.S.), the XANES edge position significantly shifts to lower energy and the sharp pre-edge feature is absent. These XANES features are consistent with a zerovalent metallic iron as the dominant iron phase. Upon subsequent reoxidation (350 °C ReOx), the XANES edge position is not fully recovered, indicating an irreversible change to the bulk iron phase and a lower average oxidation state. The EXAFS data

DOI: 10.1021/acscatal.6b01281
ACS Catal. 2016, 6, 4786−4798

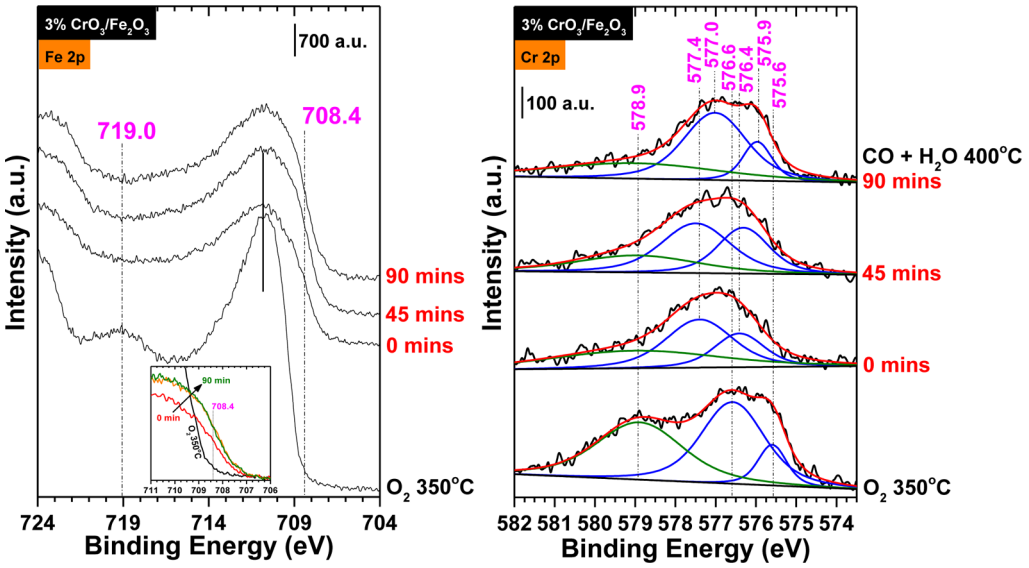

Figure 2. In situ NAP-XPS Fe 2p (left) and Cr 2p (right) spectra of 3% CrO_3/Fe_2O_3 during the WGS reaction at 400 °C, 1.0 Torr H_2O, and 0.5 Torr CO. Fe 2p Inset: magnified region containing the 708.4 eV shoulder.

before reaction (Figure S12B in the Supporting Information) similarly suggest the presence of a Fe_2O_3 bulk phase. The spectrum during the reaction indicates that a large fraction of zerovalent metallic iron exists, due to the appearance of a large Fe−Fe peak at ∼1.8 Å, and a small fraction of an iron oxide phase, due to the low-*R* peak at ∼1.1 Å in the Fe−O bond region. The lack of high-*R* peaks in the catalyst spectrum (high-*R* peaks observed with the Fe^0 reference compound) indicates an amorphous phase without long-range order. After reaction, the EXAFS spectrum is not completely recovered upon reoxidation, exhibiting a shift in the Fe^{oct}−Fe^{oct} peak (oct = octahedral coordination) and a broad shoulder between 1.5 and 2.0 Å. The corresponding MS signal (Figure S12C in the Supporting Information) shows that steady-state production of CO_2 and H_2 begins at ∼70 min, confirming that the WGS is occurring and that the XAS measurements were taken under steady-state reaction conditions.

The Cr and Fe K-edge XANES spectra for the supported 3% CrO_3/Fe_2O_3 catalyst before, during, and after the WGS reaction are presented in Figure 1A,B. Before the reaction, the Cr K-edge XANES pre-edge peak indicates that the catalyst possesses predominantly Cr^{6+}, which decreases in intensity upon heating to 350 °C for pretreatment (350 °C Ox). During the reaction (WGS S.S.), the sharp pre-edge peak is lost and the edge shifts to lower energies, indicating the reduction of Cr^{6+} to Cr^{3+} (near edge peak at ∼6011 eV from Cr^{3+}). After reoxidation, the catalyst contains an even larger fraction of Cr^{3+}. A small bump at the Cr^{6+} pre-edge peak position during and after reaction may indicate that a small amount of Cr^{6+} is present. The Fe K-edge XANES spectra before the reaction (Figure 1B, ambient and 350 °C Ox) are consistent with an Fe_2O_3 bulk phase, while the spectrum during the reaction shifts to lower energies by ∼1.5 eV, which is consistent with an Fe_3O_4 phase on the basis of reference compounds (Figure S10 in the Supporting Information). The Fe K-edge position is recovered upon a postreaction reoxidation treatment, indicating that the phase change is reversible. The EXAFS data before reaction, in Figure 1C, similarly suggest an Fe_2O_3 phase, while the spectrum during the reaction shows an increase in the ∼3.2 Å shoulder from Fe^{oct}−Fe^{tetr} bonds (tetr = tetrahedral coordination), consistent with the cubic spinel structure of an Fe_3O_4 phase. Postreaction reoxidation treatment recovers the original intensity of the Fe_2O_3 peaks. The corresponding MS data in Figure 1D indicates that steady-state production of CO_2 and H_2 begins at ∼40 min, confirming that the XAS measurements were taken under steady-state WGS reaction conditions. Results for the supported 9% CrO_3/Fe_2O_3 catalyst, given in Figure S13 in the Supporting Information, are qualitatively the same and provide the same conclusions.

3.3.4. In Situ Ambient-Pressure X-ray Photoelectron Spectroscopy (AP-XPS). Evolution of the oxidation states of the catalyst atoms in the surface region (1−3 nm) during the reaction were probed by in situ AP-XPS experiments performed at 400 °C. Results from a WGS feed with H_2O:CO = 2 are given in Figure 2 and Figure S15 in the Supporting Information for supported 3% CrO_3/Fe_2O_3 and 9% CrO_3/Fe_2O_3 catalysts, respectively. Initially, the Fe 2p region in Figure 2 (left, O_2 treatment at 350 °C) is indicative of a Fe_2O_3 phase, as previously discussed in section 3.1. During the reaction, the 719 eV satellite peak vanishes and the large Fe^{3+} $2p_{3/2}$ peak at ∼710.8 eV broadens. Likely, the broadening of the photoemission feature at ∼710.8 eV results from the appearance of a shoulder at 709−708 eV during the reaction, which indicates the presence of Fe^{2+} in a Fe_3O_4 or FeO phase, typically located at 708.4 eV.[87] As shown in Figure 2, the photoemission feature of the Cr 2p region (right, O_2 350 °C) reveals a contribution from Cr^{6+} (578.9 eV), with a fraction of 0.44, and Cr^{3+} (576.6 and 575.6 eV), with a fraction of 0.56, during pretreatment at 350 °C in O_2 before the reaction, as previously discussed in section 3.1. During the reaction, the fraction of the Cr^{6+} peak at 578.9 eV decreases to as low as 0.27. In addition, the position of the main Cr^{3+} peaks shifts to 577.4/576.4 eV from 0 to 45 min and then to 577.0/575.9 eV at 90 min. These peak shifts suggest that the local chemical environment of Cr^{3+} changes from Cr^{3+} solely coordinating with oxygen atoms to Cr^{3+} binding to lattice oxygen atoms and surface OH groups at 45 min and then to Cr^{3+} in a chemical environment similar to that of $FeCr_2O_4$ at 90 min.[87] Results for the supported 9% CrO_3/Fe_2O_3 catalyst, given in Figure S15, are similar to those for the supported 3% CrO_3/Fe_2O_3 catalyst. The catalysts, however,

DOI: 10.1021/acscatal.6b01281
ACS Catal. 2016, 6, 4786−4798

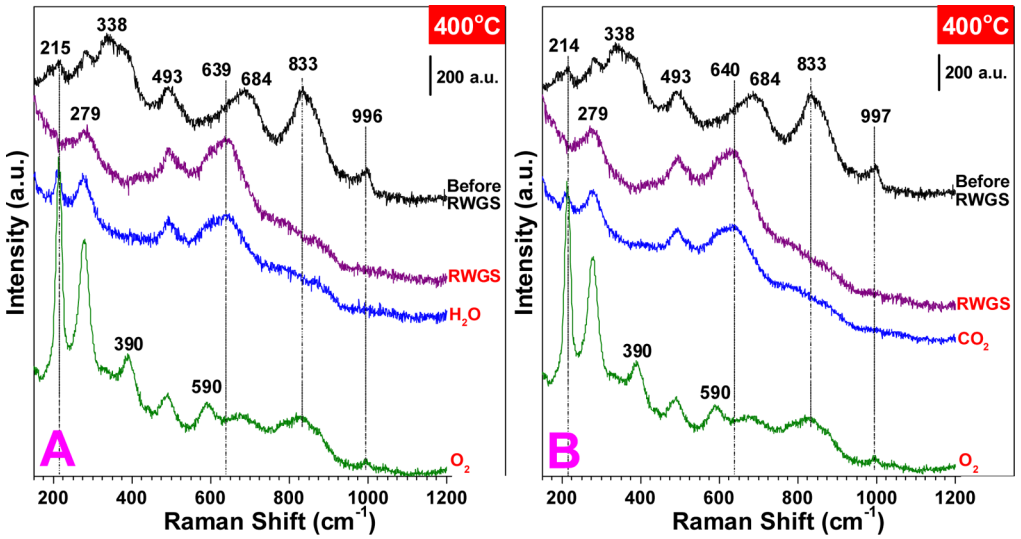

Figure 3. In situ Raman spectroscopy before, during, and after the RWGS reaction with a supported 9% CrO_3/Fe_2O_3 catalyst: (A) 2.5% H_2O/Ar oxidizing treatment after the RWGS reaction; (B) 33% CO_2/Ar oxidizing treatment after the RWGS reaction.

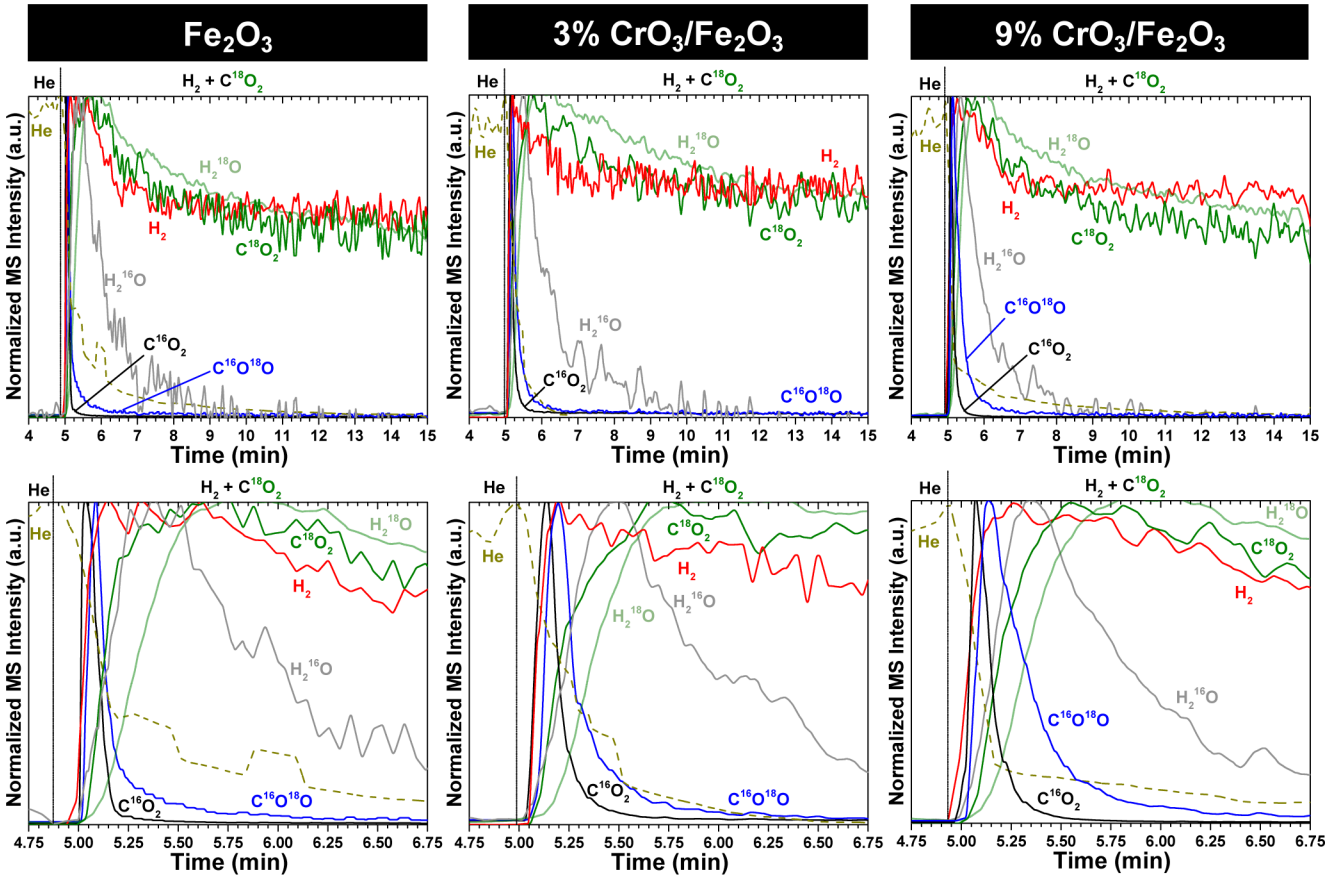

Figure 4. RWGS $C^{16}O_2/C^{18}O_2$ isotope exchange with Fe_2O_3 and *x*% CrO_3/Fe_2O_3 supported catalysts: (top row) normalized MS signals; (bottom row) magnified region.

differ in the extent of reduction of Fe_2O_3 to the Fe_3O_4 or FeO phase (reduction of the 3% CrO_3/Fe_2O_3 catalyst is much less than for the 9% CrO_3/Fe_2O_3 catalyst, which has a much smaller 708.4 eV shoulder). In addition, the atomic fraction of Cr^{6+} decreases to 0.21 during the reaction for the supported 9% CrO_3/Fe_2O_3 catalyst.

3.3.5. In Situ Raman Spectroscopy during Redox Cycles. After activation of the supported 9% CrO_3/Fe_2O_3 catalyst under the RWGS reaction conditions, reoxidation of the catalyst with H_2O or CO_2 gases was investigated and the results are given in Figure 3. During the RWGS reaction, the catalyst transforms into the Fe_3O_4 bulk phase (Raman bands at 279, 493, and 640 cm^{-1}) and the surface chromia species (Raman band at ~997 cm^{-1}) become reduced. After the RWGS, a feed of 2.5% H_2O/He or 33% CO_2/He was fed into the reactor to determine if either molecule could reoxidize the bulk iron oxide

DOI: 10.1021/acscatal.6b01281
ACS Catal. 2016, 6, 4786−4798

Table 2. RWGS Activity, Number of Sites (Ns: n(^{16}O)), Density of Sites, and Turnover Frequencies (TOFs)

catalyst	RWGS activity (10^{-6} mol/(s g))	Ns: $n(^{16}O)$ (10^{-3} mol/g)	density of Ns (^{16}O atoms/nm^2)	TOF (10^{-3} s^{-1})
Fe_2O_3	5.5	1.0	7	5.5
3% CrO_3/Fe_2O_3	6.0	1.1	8	5.4
9% CrO_3/Fe_2O_3	5.6	2.4	17	2.3

Scheme 1. Diagram of the Surface and Bulk Molecule Structures of the Supported CrO_3/Fe_2O_3 Catalyst before and during the WGS Reaction

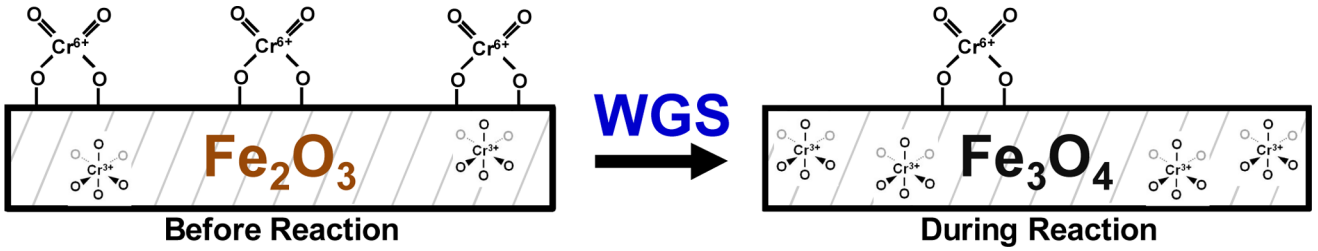

phase and surface dioxo $(O{=})_2Cr^{6+}O_2$ species. Under the H_2O feed at 400 °C (Figure 3A), a band from α-Fe_2O_3 (215 cm^{-1}) appears, indicating that the bulk iron oxide phase was partially reoxidized, but the Raman band for the surface dioxo $(O{=})_2Cr^{6+}O_2$ species (993 cm^{-1}), however, is not present. Upon exposure of the catalyst to CO_2 after the RWGS reaction at 400 °C (Figure 3B), the surface dioxo $(O{=})_2Cr^{6+}O_2$ species (997 cm^{-1}) is again not present and bulk iron oxide bands from both Fe_3O_4 (645 cm^{-1}) and α-Fe_2O_3 (214 cm^{-1}) are present. The surface dioxo $(O{=})_2Cr^{6+}O_2$ species (997 cm^{-1}) are only partially recovered upon exposure to a 10% O_2/Ar feed. Although H_2O and CO_2 are sufficiently oxidizing for oxidation of the bulk Fe_3O_4 phase to Fe_2O_3, both H_2O and CO_2 are not sufficiently strong oxidizing agents for the reoxidation of Cr^{3+} present in WGS activated chromium−iron oxide catalysts back to Cr^{6+}.

3.3.6. $C^{16}O_2/C^{18}O_2$ Isotope Exchange during RWGS. The $C^{16}O_2/C^{18}O_2$ isotope switching was performed with bulk Fe_2O_3 and supported 3% and 9% CrO_3/Fe_2O_3 catalysts during the RWGS reaction to gain insights into the oxygen exchange process taking place during the reaction, and the results are presented in Figure 4. The catalysts were initially equilibrated under a typical RWGS feed, flushed with helium, and then exposed to an isotopic H_2 + $C^{18}O_2$ RWGS feed. For the bulk Cr-free iron oxide catalyst, after the $C^{16}O_2/C^{18}O_2$ isotope switch, the first observable products were $C^{16}O_2$ and $H_2{}^{16}O$, closely followed by the mixed oxygen $C^{16}O^{18}O$ isotope (note that the transient CO isotope signals are not reliable because of CO_2 cracking in the MS). The isotopic product $H_2{}^{18}O$ is formed last. The transient production and decay of $C^{16}O_2$ and $C^{16}O^{18}O$ are similar, while only the production of the water $H_2{}^{16}O$ isotope is similar. The complete decays of the $C^{16}O_2$ and $C^{16}O^{18}O$ isotopes are rapid, <2 min after exchange, in comparison to $H_2{}^{16}O$, ~5 min after exchange.

The $C^{16}O_2/C^{18}O_2$ isotope exchange experiment during the RWGS reveals that the amount of ^{16}O being supplied by the lattice of the iron−chromium oxide catalyst ($C^{16}O^{18}O$, $H_2{}^{16}O$, and $C^{16}O_2$ as well as undetectable $C^{16}O$) is finite and small, since most of the oxygen exchange occurs within ~2 min. The number of ^{16}O* atoms participating during the $C^{16}O_2/C^{18}O_2$ isotope exchange experiment were quantified by integration of the signals of ^{16}O-containing products (sum of 2 $C^{16}O_2$, $C^{18}O^{16}O$, and $H_2{}^{16}O$). The RWGS activities and turnover frequencies on the basis of a surface O* as the most abundant reactive intermediate (MARI) are presented in Table 2. The overall catalyst activity (H_2O mol/(g s)) is virtually the same with or without the addition of chromia to iron oxide; however, the number of participating ^{16}O atoms (Ns = O atoms/g) increases by 2.4. The corresponding TOF values (TOF = activity/Ns) indicate that the specific TOF value for chromium−iron oxide catalyst is the same as that for the Cr-free iron oxide catalyst up to the initial monolayer coverage (3% CrO_3/Fe_2O_3), after which additional chromium causes a decrease in the TOF by a factor of ~2.3. Thus, Cr is a textural promoter that increases the number of catalytic active sites but does not chemically promote the WGS reaction by iron oxide. The slightly lower TOF for the 9% CrO_3/Fe_2O_3 catalyst may indicate a slight retardation of the specific activity in the presence of significant chromia.

4. DISCUSSION

4.1. Catalyst Structures in Initial Oxidized Catalyst.

4.1.1. Bulk Structures. The bulk iron oxide phase is initially present as Fe_2O_3 for all catalysts. For the supported CrO_3/Fe_2O_3 catalysts, the iron oxide phase was present only as γ-Fe_2O_3 (see Figure S2 in the Supporting Information); however, for pure iron oxide the phase can be a mixture of α- and γ-Fe_2O_3. The absence of discrete Cr_2O_3 nanoparticles for most chromium oxide loadings greater than monolayer coverage for the supported CrO_3/Fe_2O_3 catalysts (see Figure S2) suggests Cr dissolution into the Fe_2O_3 support. This is further supported by the significant amount of Cr^{3+} present in the in situ XANES and XPS (Figures S3 and S4 in the Supporting Information) of the supported 9% CrO_3/Fe_2O_3 catalyst but not in the in situ XANES for the monolayer supported 3% CrO_3/Fe_2O_3 catalyst. In addition, just heating chromium−iron oxide catalysts under oxidizing conditions increases the concentration of Cr^{3+} in the bulk Fe_2O_3 lattice (see Figure 1). Dissolution of chromium oxide into the iron oxide bulk lattice as Cr^{3+} is known to displace Fe^{2+}/Fe^{3+} from octahedral sites and expose the iron oxide surface.[11,13−17] A diagram of the bulk structure of the initial oxidized chromium−iron oxide catalyst is given in Scheme 1.

4.1.2. Surface Structures. The initial oxidized chromium−iron oxide catalysts possess a surface chromia phase primarily present as dioxo $(O{=})_2Cr^{6+}O_2$ surface species, but a small amount of surface mono-oxo $O{=}CrO_4$ species are also present (see Figure S1 in the Supporting Information). The separation

DOI: 10.1021/acscatal.6b01281
ACS Catal. 2016, 6, 4786−4798

of ~14 cm^{-1} between the symmetric and asymmetric vibrations of O═Cr═O observed in the Raman and IR spectra, respectively, also matches the vibrational rules for dioxo metal oxides.[11,13−17,100,101] The surface chromia species on Fe_2O_3 are metastable, since their total concentration decreases at elevated temperatures in oxidizing environments (see Figure 1). There appears to be an equilibrium ratio of Cr^{6+}/Cr^{3+} in the surface region, as indicated by nearly identical atomic fractions observed in the in situ XPS (Figure S4 in the Supporting Information). The surface chromia species anchor to the surface of Fe_2O_3 by titrating the iron oxide surface hydroxyls (see Figure S1). A diagram of the major surface chromia species on iron oxide before the reaction is given in Scheme 1.

4.2. Catalyst Structures during the WGS/RWGS Reactions. *4.2.1. Bulk Structures.* During the WGS/RWGS reactions, the thermodynamically stable Fe_3O_4 bulk phase is present in all chromium−iron oxide catalysts (see Figure 1 and Figures S9−S13 and S15 in the Supporting Information), even under very reducing conditions (Raman, H_2:CO_2 = 4 for RWGS). For the Cr-free iron oxide catalyst, the metallic Fe^0 bulk phase predominates (EXAFS, see Figure S12 in the Supporting Information). This over-reduction of iron oxide is well-known in the literature, indicating the need for very careful catalyst activation.[1,2,4] The presence of Cr^{3+} in the bulk iron oxide lattice retards the formation of metallic Fe^0 (EXAFS, see Figure 1 and Figures S12 and S13). The dissolution of Cr^{3+} into the iron oxide bulk lattice at elevated temperatures and WGS/RWGS reaction conditions is indicated by the increased Cr^{3+} signal (EXAFS, see Figure 1). Reoxidation with O_2 after RWGS only partially reoxidizes the chromia to surface Cr^{6+} (EXAFS and Raman, see Figures 1 and 3 and Figure S13) and is consistent with the trapping of Cr^{3+} in the iron oxide bulk lattice.[11,13−17] The Cr^{3+} sites in the iron oxide bulk lattice during the WGS/RWGS reactions are responsible for stabilization of the Fe_3O_4 phase (minimization of metallic Fe^0 phase) and the enhanced BET surface area (see Table 1). A diagram of the bulk structures of the chromium−iron oxide catalysts during the WGS/RWGS reactions is given in Scheme 1.

4.2.2. Surface Structures. The surface of chromium−iron oxide catalysts during WGS/RWGS contains both exposed Cr and Fe sites. Although most of the chromia is dissolved as Cr^{3+} in the Fe_3O_4 bulk lattice during WGS/RWGS, a small amount of Cr^{6+} also remains on the surface of the catalyst (see Figure 2). The Raman band for the dioxo surface Cr^{6+} species (997 cm^{-1}) reappears, but with a low intensity, after the RWGS reaction by reoxidation with O_2, indicating the presence of some reduced Cr^{3+} species either on the topmost surface or in the surface region (several nanometers in depth) of the chromium−iron oxide catalyst during the WGS/RWGS reactions. The minor amount of surface chromia species on the chromium−iron oxide catalyst during the WGS/RWGS reactions suggests that the chromium−iron oxide surface is dominated by the Fe_3O_4 surface features of Fe^{2+} and Fe^{3+} in octahedral and tetrahedral coordinations (in situ XPS, Figure 2 and Figure S15 in the Supporting Information). A diagram of the surface structure of the chromium−iron oxide catalyst during the WGS/RWGS reactions is depicted in Scheme 1. For pure iron oxide, it is hypothesized that the fraction of α- and γ-Fe_2O_3 phases before the reaction will influence the reactivity of the catalyst, as either phase may promote specific stoichiometries on the catalyst surface.

4.3. Catalytic Active Sites during the WGS/RWGS Reactions. Although the surface of the chromium−iron oxide catalyst during the WGS/RWGS reactions contains mostly Fe and a minor amount of Cr^{6+}/Cr^{3+}, only the surface FeO_x sites are involved in the redox cycle. The inability to reoxidize the surface Cr^{3+} sites with both H_2O and CO_2, the oxidizing agents during the WGS/RWGS reactions suggests that surface Cr^{3+} sites cannot participate in the WGS/RWGS reactions (see Figure 3) while Cr^{6+} is a spectator and may even retard the catalytic activity slightly, as indicated by decreases in the TOF upon chromium addition (Table 2). This leaves only the surface FeO_x as being the catalytic active sites for the WGS/RWGS reactions, since Fe is reoxidized by both H_2O and CO_2 (see Figure 3) and Cr-free iron oxide is also able to perform the WGS/RWGS reactions.

The HT-WGS catalysis literature is conflicted about the role of chromium in the chromium−iron oxide catalysts. Traditionally, it was concluded that the only function of chromium is as a textural promoter to increase the surface area of iron oxide, but the promotion mechanism was not known.[1,2,4,7,14,21−25] Multiple mechanisms, however, have been proposed for Cr stabilization of iron oxide and its catalytic role: chromia forms discrete Cr_2O_3 particles on Fe_3O_4, preventing agglomeration of iron oxide,[73,75] enrichment of Cr^{3+} in the surface region is more thermodynamically stable than iron oxide and reduces ion diffusion and sintering effects,[23] dissolved Cr^{3+} occupies octahedral sites in the bulk Fe_3O_4 lattice that prevent sintering by forcing bulk FeO_6 sites to occupy bulk FeO_4 sites,[102] and the chromia redox cycle of $Cr^{3+} \Leftrightarrow Cr^{6+}$ promotes the $Fe^{2+} \Leftrightarrow Fe^{3+}$ redox cycle of the Fe_3O_4 phase.[19] The proposal that the $Cr^{3+} \Leftrightarrow Cr^{6+}$ redox cycle promotes the $Fe^{2+} \Leftrightarrow Fe^{3+}$ redox cycle of the Fe_3O_4 phase is not supported by the current findings, since the chromia redox cycle does not operate during the WGS/RWGS reactions (see Figure 3). The current Raman studies also demonstrate that discrete Cr_2O_3 particles are not present on Fe_3O_4 because of facile dissolution of Cr^{3+} in the iron oxide bulk lattice (see Figures S2 and S9−S11 in the Supporting Information) and negate this antiagglomeration proposal. Analogously, a significant surface-enriched chromia phase is not present during the reaction and, thus, surface chromia probably cannot be responsible for preventing sintering of iron oxide. The only stabilization mechanism consistent with the experimental findings is that dissolved Cr^{3+} occupies octahedral sites in the bulk Fe_3O_4 lattice which prevent sintering by forcing bulk FeO_6 sites to occupy bulk FeO_4 sites. The current operando EXAFS findings (see Figure 1 and Figures S12 and S13 in the Supporting Information) also reveal that the Cr^{3+} species dissolved in the iron oxide bulk lattice suppress formation of metallic Fe^0 that is more prone to sintering than iron oxides.

The isotope switch experiment (Figure 4) provides quantification of the number of exchangeable active O* atoms participating in the RWGS reaction under realistic reaction conditions and using the same reaction gas composition as for the in situ/operando spectroscopy experiments. Previous efforts utilized adsorption and relaxation kinetics of CO/CO_2 and H_2/H_2O gas mixtures to quantify the number of O* atoms and concluded that they comprised of ~10−20% of the surface area under the conditions studied (pressures <40 kPa or ~0.4 atm and temperatures of ~340−400 °C).[12,57,58,61−65] It has been demonstrated that the Fe_3O_4 (111) surface possess 3/4 monolayer of oxygen atoms (14.2 atoms/nm^2) and 1/4 monolayer of iron atoms that can be

DOI: 10.1021/acscatal.6b01281
ACS Catal. 2016, 6, 4786−4798

saturated with hydroxyls (4.7 atoms/nm^2), which gives an overall density of 18.9 oxygen atoms/nm^2.[103,104] Results of the current isotope exchange give an experimental value ranging from 7 to 17 ^{16}O atoms/nm^2, indicating that nearly the entire surface layer can participate in the HT-WGS reaction and that previous methods have significantly undercounted the number of sites by nearly 1 order of magnitude. It is likely that undercounting in the literature is due to the use of high-vacuum systems that can alter the catalyst surface with multiple evacuations, low pressures during counting steps (<40 kPa), and the use of only half of the WGS reactants/products (CO/CO_2 or H_2/H_2O mixtures) during counting, which does not simulate the oxyreduction potential of the full WGS mixture.

4.4. Surface Reaction Intermediates during the WGS/RWGS Reactions. There have been many surface reaction intermediates proposed for the WGS reaction, with surface carbonates and formates being the most popular. Although surface intermediates have been observed for the low-temperature WGS (Cu−Zn−Al) catalysts, there has been no direct evidence for surface reaction intermediates during the high-temperature WGS/RWGS reactions,[1,2,4] only some indirect evidence of carbonates from isotopic ($^{18}O_2$ and $C^{18}O_2$) temperature-programmed desorption experiments.[57] This is related to the short lifetime and low concentrations of the surface intermediates during high-temperature WGS/RWGS that prevents their observation. For example, the efficient exchange of ^{18}O from $C^{18}O_2$ with the chromium−iron oxide catalyst to form $C^{16}O_2$ and $C^{18}O^{16}O$, as observed during isotope exchange (Figure 4), suggests that some exchange proceeds via surface carboxylate/carbonate intermediates, but these intermediates can only be detected spectroscopically at subambient temperatures, where they have a long lifetime (see Figures S6 and S7 in the Supporting Information). Another possible reason for the lack of detection of surface intermediates during high-temperature WGS/RWGS is the loss of transparency of the catalysts with respect to IR. Similarly, surface formate intermediates were observed on the iron and chromium−iron oxide catalysts upon adsorption of CO_2 (see Figure S6 in the Supporting Information), HCOOH (see Figure S8 in the Supporting Information) and CH_3OH (see Figure S18 in the Supporting Information), but at temperatures lower than those typically encountered for the high temperatures of ∼400 °C WGS/RWGS reactions, since surface formates are not stable above 325 °C (see Figure S8 in the Supporting Information). Even performing the WGS reaction at lower temperatures of 200−325 °C does not yield the IR spectra of surface formate intermediates (see Figures S16 and S17 in the Supporting Information). The lack of observation of surface reaction intermediates during high-temperature WGS/RWGS is clouded by the possible loss of the IR signal from the chromium−iron oxide catalyst's reduced state. The most abundant reactive intermediate is actually the surface O* sites on the catalysts, as shown by the isotope exchange analysis.

4.5. WGS/RWGS Reaction Mechanisms. Two reaction mechanisms have been proposed for the high-temperature WGS/RWGS reactions: associative mechanism involving a surface reaction intermediate and a redox mechanism involving oxygen exchange between the gases and the iron oxide based catalyst.[1,2,4] As already indicated, there is no direct evidence for the associative mechanism, since surface intermediates are not detectable on either iron oxide or chromium−iron oxide catalysts during high-temperature WGS/RWGS (see Figures S16 and S17 in the Supporting Information). The associative mechanism may be operating during high-temperature WGS/RWGS, but at present it has not been directly proven.

There is direct evidence, however, that the redox mechanism is operating during the high-temperature RWGS reaction from transient $C^{16}O_2/H_2$ → inert flush → $C^{18}O_2/H_2$ experiments. The isotope switch experiments demonstrate that the RWGS reaction is proceeding via the redox mechanism, since the isotope switch readily produces ^{16}O-containing reaction products ($C^{16}O_2$, $C^{16}O^{18}O$, and $H_2{}^{16}O$) in the $C^{18}O_2/H_2$ reaction environment and the exchange is nearly complete within 2 min. The short exchange time indicates that a surface Mars−van Krevelen (MVK) reaction mechanism is taking place where only the surface layer is exchanging oxygen atoms, rather than a bulk MVK mechanism where complete exchange only occurs after an extended period of time. The formation of the $C^{16}O_2$ and $C^{16}O^{18}O$ products is not only from the RWGS, since they can also form when only $C^{18}O_2$ is exchanged with the equilibrated ^{16}O-containing catalyst. This suggests that the CO_2 exchange also takes place via short-lived surface carboxylates/carbonates, which is a parallel oxygen exchange pathway.[57] Formation of $H_2{}^{16}O$ before $H_2{}^{18}O$ in the presence of $C^{18}O_2/H_2$ is consistent with a redox process taking place during RWGS. Furthermore, the isotope switch experiment also provides quantification of the number of exchangeable active O* atoms participating in the RWGS reaction under realistic reaction conditions.

4.6. Structure−Activity Relationships. The catalytic active sites during the WGS/RWGS are O* atoms affiliated with iron oxide sites in the outermost surface layer. This conclusion is supported by (i) the low concentration of surface chromia sites on the equilibrated chromium−iron oxide catalyst because of significant dissolution of Cr^{3+} into the iron oxide bulk lattice (see Figures 1−3 and Figures S2−S4, S9−S13, and S15) in the Supporting Information, (ii) the ability of Cr-free iron oxide to perform HT-WGS/RWGS (see Figure 4 and Figures S9 and S12 in the Supporting Information), (iii) the reoxidation of Fe^{2+} to Fe^{3+} with CO_2 and H_2O (see Figure 3), (iv) the inability to reoxidize Cr^{3+} back to Cr^{6+} with CO_2 and H_2O (see Figure 3), (v) the inability to extensively reoxidize Cr^{3+} back to surface Cr^{6+} even with O_2 after WGS/RWGS due to its dissolution in the iron oxide bulk lattice (see Figures 1 and 3 and Figures S13, S19, and S20 in the Supporting Information), and (vi) lack of an increase and even a slight decrease in TOF for Cr-promoted iron oxide catalysts (see Table 2). Thus, the only function of the chromia promoter is to stabilize the Fe_3O_4 phase with a higher surface area (textural promoter), which is in agreement with the current accepted mechanism in the literature.

5. CONCLUSIONS

A series of supported CrO_3/Fe_2O_3 catalysts prepared by incipient wetness impregnation were investigated for the high-temperature WGS reaction as a function of chromia loading and extensively characterized. Characterization before reaction by in situ IR, Raman, XAS, and AP-XPS revealed that the catalyst contains a 2-D surface phase consisting primarily of dioxo $(O{=})_2Cr^{6+}O_2$ species and a bulk γ-Fe_2O_3 phase with some Cr^{3+} substituted into the bulk lattice. The adsorption of probe molecules was monitored using in situ IR spectroscopy and revealed various adsorbed carbonates and formates from CO and CO_2 adsorption and adsorbed formates from HCOOH adsorption directly. Surface formate species were thermody-

DOI: 10.1021/acscatal.6b01281
ACS Catal. 2016, 6, 4786−4798

namically preferred and were demonstrated to be stable up to 250−325 °C on the catalyst surface.

Characterization during the high-temperature WGS reaction by operando IR, Raman, XAS, and in situ AP-XPS revealed that the crystalline Fe_3O_4 phase is the active bulk phase and surface dioxo $(O{=})_2Cr^{6+}O_2$ species become reduced during reaction to Cr^{3+} and migrate into the bulk iron oxide lattice ($Fe_{3-x}Cr_xO_4$). In situ AP-XPS data have revealed that a minor amount of Cr^{6+} species may remain on the catalyst surface under the reaction conditions. Corresponding in situ Raman and operando IR redox cycles indicate that the trace surface Cr^{6+} is a spectator species during the WGS reaction. Isotope exchange experiments during the RWGS indicate that a surface Mars−van Krevelen mechanism is occurring and the catalytic active sites during the WGS/RWGS are surface O* atoms affiliated with iron oxide sites in the surface region. The chromia promoter only increases the population of sites, and it does not chemically promote the reaction. Furthermore, quantification of the active O* atoms indicates that previous titration methods have been undercounting the number of sites by nearly 1 order of magnitude. These new insights have led to a modern fundamental understanding of the high-temperature WGS catalyst.

■ ASSOCIATED CONTENT

Supporting Information

The Supporting Information is available free of charge on the ACS Publications website at DOI: 10.1021/acscatal.6b01281.

In situ IR and Raman spectroscopy, in situ XANES/EXAFS, and in situ XPS of the dehydrated catalyst, XANES and EXAFS reference compounds, in situ IR spectroscopy during adsorption of probe molecules CO, CO_2, HCOOH, and CH_3OH, operando Raman spectroscopy during the water-gas shift reaction, operando XANES/EXAFS during the water-gas shift reaction, in situ AP-XPS during the water-gas shift reaction, operando IR spectroscopy during the water-gas shift reaction, and 8) operando IR spectroscopy during redox cycles (PDF)

■ AUTHOR INFORMATION

Corresponding Authors

*E-mail for C.J.K.: cjk@cummins.com.

*E-mail for I.E.W.: iew0@lehigh.edu.

Present Addresses

[⊥]Cummins Emission Solutions, Stoughton, WI 53589, USA.

[#]Department of Chemistry, University College London, London WC1E 6BT, U.K.

Notes

The authors declare no competing financial interest.

■ ACKNOWLEDGMENTS

The authors gratefully acknowledge help of Relja Vasic and Nebojsa Marinkovic with synchrotron measurements at Brookhaven National Laboratory. C.J.K. and I.E.W. gratefully acknowledge support by the NSF IREE Award No. 0609018 and NSF Award No. 1511689. A.I.F. acknowledges support by the U.S. DOE Grant No. DE-FG02-03ER15476. Beamline X19A of the NSLS is supported in part by the U.S. DOE Grant No. DE-FG02-05ER15688. The NSLS is supported by U.S. DOE Contract No. DE-AC02-98CH10886. F.T. acknowledges support by the Chemical Sciences, Geosciences and Biosciences Division, Office of Basic Energy Sciences, Office of Science, U.S. Department of Energy, under Grant No. DE-SC0014561.

■ REFERENCES

(1) Rhodes, C.; Hutchings, G.; Ward, A. *Catal. Today* **1995**, *23*, 43−58.

(2) Ratnasamy, C.; Wagner, J. P. *Catal. Rev.: Sci. Eng.* **2009**, *51*, 325−440.

(3) Brenna, G. *New Catalyst for the H2 Production By Water-Gas Shift Reaction Processes*; Università di Bologna: Bologna, Italy, 2010.

(4) Newsome, D. S. *Catal. Rev.: Sci. Eng.* **1980**, *21*, 275−318.

(5) Bosch, C.; Wild, W. United States Patent 1,115,776, 1914.

(6) Rodriguez, J. A.; Hanson, J. C.; Stacchiola, D.; Senanayake, S. D. *Phys. Chem. Chem. Phys.* **2013**, *15*, 12004−12025.

(7) Ladebeck, J. R.; Wagner, J. P. In *Handbook of Fuel Cells-Fundamentals, Technology and Applications*; Vielstich, W., Lamm, A., Gasteiger, H. A., Eds.; Wiley: Chichester, U.K., 2003; Vol. 3, pp 190−201.

(8) Zhu, M.; Wachs, I. E. *ACS Catal.* **2016**, *6*, 722−732.

(9) Lee, D.-W.; Lee, M. S.; Lee, J. Y.; Kim, S.; Eom, H.-J.; Moon, D. J.; Lee, K.-Y. *Catal. Today* **2013**, *210*, 2−9.

(10) Wachs, I. E.; Keturakis, C. J. In *Comprehensive Inorganic Chemistry*; Schlögl, R., Ed.; Elsevier: Waltham, MA, 2013; Vol. 7, pp 131−151.

(11) Filoti, G.; Nistor, L.; Doca, I.; Brasoveanu, I.; Spanu, V.; Teodorescu, V.; Rotaru, P.; Blejoiu, S. I. *Rev. Roum. Chim.* **1979**, *24*, 1101−1105.

(12) Kubsh, J. E.; Chen, Y.; Dumesic, J. A. *J. Catal.* **1981**, *71*, 192−200.

(13) Kundu, M. L.; Sengupta, A. C.; Maiti, G. C.; Sen, B.; Ghosh, S. K.; Kuznetsov, V. I.; Kustova, G. N.; Yurchenko, E. N. *J. Catal.* **1988**, *112*, 375−383.

(14) Pereira, A.; Berrocal, G.; Marchetti, S.; Albornoz, A.; De Souza, A.; Rangel, M. *J. Mol. Catal. A: Chem.* **2008**, *281*, 66−72.

(15) Reddy, G. K.; Gunasekera, K.; Boolchand, P.; Dong, J.; Smirniotis, P. G. *J. Phys. Chem. C* **2011**, *115*, 7586−7595.

(16) Reddy, G. K.; Gunasekara, K.; Boolchand, P.; Smirniotis, P. G. *J. Phys. Chem. C* **2011**, *115*, 920−930.

(17) Reddy, G. K.; Boolchand, P.; Smirniotis, P. G. *J. Phys. Chem. C* **2012**, *116*, 11019−11031.

(18) Keiski, R. L.; Salmi, T. *Appl. Catal., A* **1992**, *87*, 185−203.

(19) Natesakhawat, S.; Wang, X.; Zhang, L.; Ozkan, U. S. *J. Mol. Catal. A: Chem.* **2006**, *260*, 82−94.

(20) Lee, J. Y.; Lee, D.-W.; Hong, Y.-K.; Lee, K.-Y. *Int. J. Hydrogen Energy* **2011**, *36*, 8173−8180.

(21) Martis, V.; Oldman, R.; Anderson, R.; Fowles, M.; Hyde, T.; Smith, R.; Nikitenko, S.; Bras, W.; Sankar, G. *Phys. Chem. Chem. Phys.* **2013**, *15*, 168−175.

(22) Quadro, E. B.; Dias, M. d. L. R.; Maria, A.; Amorim, M.; Rangel, M. d. C. *J. Braz. Chem. Soc.* **1999**, *10*, 51−59.

(23) Edwards, M. A.; Whittle, D. M.; Rhodes, C.; Ward, A. M.; Rohan, D.; Shannon, M. D.; Hutchings, G. J.; Kiely, C. J. *Phys. Chem. Chem. Phys.* **2002**, *4*, 3902−3908.

(24) Martos, C.; Dufour, J.; Ruiz, A. *Int. J. Hydrogen Energy* **2009**, *34*, 4475−4481.

(25) Khaleel, A.; Shehadi, I.; Al-Shamisi, M. *Colloids Surf., A* **2010**, *355*, 75−82.

(26) Domka, F.; Basinska, A.; Przystajko, W.; Fiedorow, R. *Surf. Technol.* **1984**, *21*, 101−108.

(27) Tsokov, P.; Blaskov, V.; Klissurski, D.; Tsolovski, I. *J. Mater. Sci.* **1993**, *28*, 184−188.

(28) Rangel, M. d. C.; Sassaki, R. M.; Galembeck, F. *Catal. Lett.* **1995**, *33*, 237−254.

(29) Chen, L. S.; Lu, G. L. *J. Mater. Sci.* **1999**, *34*, 4193−4197.

(30) Kumar, P.; Idem, R. *Energy Fuels* **2007**, *21*, 522−529.

(31) Scariot, M.; Francisco, M. S. P.; Jordao, M. H.; Zanchet, D.; Logli, M. A.; Vicentini, V. P. *Catal. Today* **2008**, *133−135*, 174−180.

(32) Boudjemaa, A.; Auroux, A.; Boumaza, S.; Trari, M.; Cherifi, O.; Bouarab, R. *React. Kinet. Catal. Lett.* **2009**, *98*, 319−325.

DOI: 10.1021/acscatal.6b01281
ACS Catal. 2016, 6, 4786−4798

(33) Reddy, G. K.; Boolchand, P.; Smirniotis, P. G. *J. Catal.* **2011**, *282*, 258−269.
(34) Reddy, G. K.; Smirniotis, P. G. *Catal. Lett.* **2011**, *141*, 27−32.
(35) Meshkani, F.; Rezaei, M. *J. Ind. Eng. Chem.* **2014**, *20*, 3297−3302.
(36) Busca, G.; Lorenzelli, V. *Mater. Chem.* **1980**, *5*, 213−224.
(37) Busca, G.; Lorenzelli, V. *React. Kinet. Catal. Lett.* **1980**, *15*, 273−278.
(38) Busca, G.; Lorenzelli, V. *J. Catal.* **1980**, *66*, 155−161.
(39) Busca, G.; Lorenzelli, V. *Mater. Chem.* **1982**, *7*, 89−126.
(40) Lorenzelli, V.; Busca, G.; Sheppard, N.; Al-Mashta, F. *J. Mol. Struct.* **1982**, *80*, 181−186.
(41) Ramis, G.; Busca, G.; Lorenzelli, V. *Mater. Chem. Phys.* **1991**, *29*, 425−435.
(42) Busca, G.; Lorenzelli, V.; Ramis, G.; Willey, R. J. *Langmuir* **1993**, *9*, 1492−1499.
(43) de Faria, D.; Silva, S.; de Oliveira, M. *J. Raman Spectrosc.* **1997**, *28*, 873−878.
(44) Cornell, R. M.; Schwertmann, U. *The Iron Oxides: Structure, Properties, Reactions, Occurrences and Uses*; Wiley-VCH: Weinheim, Germany, 2003; p 703.
(45) Baltrusaitis, J.; Jensen, J. H.; Grassian, V. H. *J. Phys. Chem. B* **2006**, *110*, 12005−12016.
(46) de Smit, E.; Weckhuysen, B. M. *Chem. Soc. Rev.* **2008**, *37*, 2758−2781.
(47) Boudjemaa, A.; Daniel, C.; Mirodatos, C.; Trari, M.; Auroux, A.; Bouarab, R. *C. R. Chim.* **2011**, *14*, 534−538.
(48) Busca, G.; Lorenzelli, V. *J. Chem. Soc., Faraday Trans.* **1992**, *88*, 2783−2789.
(49) Topsoe, H.; Dumesic, J. A.; Boudart, M. *J. Phys. Colloques* **1974**, *35*, C6-411−C6-413.
(50) Cherkezova-Zheleva, Z.; Mitov, I. *J. Physics: Conf. Series* **2010**, *217*, 012044−012047.
(51) Zanchet, D.; Rodella, C. B.; Lopes, L. J. S.; Logli, M. A.; Vicentini, V. P.; Wen, W.; Hanson, J. C.; Rodriguez, J. A. *AIP Conf. Proc.* **2008**, *1092*, 25−28.
(52) Kendelewicz, T.; Kaya, S.; Newberg, J. T.; Bluhm, H.; Mulakaluri, N.; Moritz, W.; Scheffler, M.; Nilsson, A.; Pentcheva, R.; Brown, G. E. *J. Phys. Chem. C* **2013**, *117*, 2719−2733.
(53) Patlolla, A.; Carino, E. V.; Ehrlich, S. N.; Stavitski, E.; Frenkel, A. I. *ACS Catal.* **2012**, *2*, 2216−2223.
(54) Boreskov, G. K. *Discuss. Faraday Soc.* **1966**, *41*, 263−276.
(55) Muzykantov, V. S.; Popovskii, V. V.; Boreskov, G. K.; Panov, G. I.; Shkrabina, R. A. *Sov. Appl. Mech.* **1969**, *5*, 344−350.
(56) Kasatkina, L. A.; Mekipelov, V. N.; Zhivotenko, N. N. *Kinet. Katal.* **1973**, *14*, 363−371.
(57) Udovic, T. J.; Dumesic, J. A. *J. Catal.* **1984**, *89*, 314−326.
(58) Lund, C. R. F.; Kubsh, J. E.; Dumesic, J. A. In *Solid State Chemistry in Catalysis*; Grasselli, R. K., Ed.; American Chemical Society: Washington, DC, 1985; ACS Symp. Ser. *279*, pp 313−338.
(59) Rethwisch, D. G.; Dumesic, J. A. *Appl. Catal.* **1986**, *21*, 97−109.
(60) Weckhuysen, B. M.; Wachs, I. E. *J. Chem. Soc., Faraday Trans.* **1996**, *92*, 1969−1973.
(61) Kubsh, J. E.; Dumesic, J. A. *AIChE J.* **1982**, *28*, 793−800.
(62) Tinkle, M.; Dumesic, J. A. *J. Phys. Chem.* **1984**, *88*, 4127−4130.
(63) Rethwisch, D. G.; Dumesic, J. A. *Langmuir* **1986**, *2*, 73−79.
(64) Tinkle, M.; Dumesic, J. A. *J. Catal.* **1987**, *103*, 65−78.
(65) Rethwisch, D. G.; Dumesic, J. A. In *Catalytic Activation of Carbon Dioxide*; Ayers, W. M., Ed.; American Chemical Society: Washington, DC, 1988; ACS Symp. Ser. *363*, pp 102−122.
(66) Zhu, M.; Wachs, I. E. *ACS Catal.* **2016**, *6*, 1764−1767.
(67) Boreskov, G. K. *Kinet. Katal.* **1970**, *11*, 374−382.
(68) Boreskov, G. K. *Kinet. Katal.* **1980**, *11*, 312.
(69) Rethwisch, D. G.; Dumesic, J. A. *J. Phys. Chem.* **1986**, *90*, 1625−1630.
(70) Oki, S.; Mezaki, R. *J. Phys. Chem.* **1973**, *77*, 1601−1605.
(71) Armstrong, E. F.; Hilditch, T. P. *Proc. R. Soc. London, Ser. A* **1920**, *97*, 265−273.
(72) Mezaki, R.; Oki, S. *J. Catal.* **1973**, *30*, 488−489.
(73) Chinchen, G. C.; Logan, R. H.; Spencer, M. S. *Appl. Catal.* **1984**, *12*, 97−103.
(74) Chinchen, G. C.; Logan, R. H.; Spencer, M. S. *Appl. Catal.* **1984**, *12*, 69−88.
(75) Chinchen, G. C.; Logan, R. H.; Spencer, M. S. *Appl. Catal.* **1984**, *12*, 89−96.
(76) Botes, F. G. *Appl. Catal., A* **2007**, *328*, 237−242.
(77) Vimont, A.; Daturi, M.; Winfield, J. M. In *Functionalized Inorganic Fluorides: Synthesis, Characterizations & Properties of Nanostructured Solids*; Tressaud, E., Ed.; Wiley-Blackwell: Chichester, U.K., 2010; Vol. Chapter 4, pp 101−139.
(78) Lee, E.; Wachs, I. E. *J. Phys. Chem. C* **2007**, *111*, 14410−14425.
(79) Frenkel, A. I.; Wang, Q.; Marinkovic, N.; Chen, J. G.; Barrio, L.; Si, R.; Lopez-Camara, A.; Estrella, A. M.; Rodriguez, J. A.; Hanson, J. C. *J. Phys. Chem. C* **2011**, *115*, 17884−17890.
(80) Tao, F. *Chem. Commun.* **2012**, *48*, 3812−3814.
(81) Wen, C.; Zhu, Y.; Ye, Y.; Zhang, S.; Cheng, F.; Liu, Y.; Wang, P.; Tao, F. *ACS Nano* **2012**, *6*, 9305−9313.
(82) Zhang, S.; Nguyen, L.; Zhu, Y.; Zhan, S.; Tsung, C.-K.; Tao, F. *Acc. Chem. Res.* **2013**, *46*, 1731−1739.
(83) Hardcastle, F. D.; Wachs, I. E. *J. Mol. Catal.* **1988**, *46*, 173−186.
(84) Cieslak-Golonka, M. *Coord. Chem. Rev.* **1991**, *109*, 223−249.
(85) Vuurman, M. A.; Wachs, I. E.; Stufkens, D. J.; Oskam, A. *J. Mol. Catal.* **1993**, *80*, 209−227.
(86) Kagwade, S. V.; Clayton, C. R.; Halada, G. P. *Surf. Interface Anal.* **2001**, *31*, 442−447.
(87) Biesinger, M. C.; Payne, B. P.; Grosvenor, A. P.; Lau, L. W. M.; Gerson, A. R.; Smart, R. S. C. *Appl. Surf. Sci.* **2011**, *257*, 2717−2730.
(88) Guo, Q.; Moller, P. J. *Surf. Sci.* **1995**, *340*, L999−L1004.
(89) Lemire, C.; Bertarione, S.; Zecchina, A.; Scarano, D.; Chaka, A.; Shaikhutdinov, S.; Freund, H.-J. *Phys. Rev. Lett.* **2005**, *94*, 166101.
(90) Lutz, H. D.; Moller, H.; Schmidt, M. *J. Mol. Struct.* **1994**, *328*, 121−132.
(91) Oh, S. J.; Cook, D. C.; Townsend, H. E. *Hyperfine Interact.* **1998**, *112*, 59−66.
(92) Frenkel, A. I.; Cross, J. O.; Fanning, D. M.; Robinson, I. K. *J. Synchrotron Radiat.* **1999**, *6*, 332−334.
(93) Hadjiivanov, K. I.; Vayssilov, G. N. *Adv. Catal.* **2002**, *47*, 307−511.
(94) Vimont, A.; Leclerc, H.; Mauge, F.; Daturi, M.; Lavalley, J. C.; Surble, S.; Serre, C.; Ferey, G. *J. Phys. Chem. C* **2007**, *111*, 383−388.
(95) Busca, G.; Lorenzelli, V. *Mater. Chem.* **1982**, *7*, 89.
(96) Busca, G.; Lamotte, J.; Lavalley, J. C.; Lorenzelli, V. *J. Am. Chem. Soc.* **1987**, *109*, 5197−5202.
(97) Hadjiivanov, K. I.; Busca, G. *Langmuir* **1994**, *10*, 4534−4541.
(98) Glisenti, A. *J. Chem. Soc., Faraday Trans.* **1998**, *94*, 3671−3676.
(99) Landon, J.; Demeter, E.; Inoglu, N.; Keturakis, C.; Wachs, I. E.; Vasic, R.; Frenkel, A. I.; Kitchin, J. R. *ACS Catal.* **2012**, *2*, 1793−1801.
(100) Stephens, J. S.; Cruickshank, D. W. J. *Acta Crystallogr., Sect. B: Struct. Crystallogr. Cryst. Chem.* **1970**, *26*, 222−226.
(101) Busca, G. *J. Raman Spectrosc.* **2002**, *33*, 348−358.
(102) Robbins, M.; Wertheim, G. K.; Sherwood, R. C.; Buchanan, D. N. E. *J. Phys. Chem. Solids* **1971**, *32*, 717−729.
(103) Sharp, J. C.; Yao, Y. X.; Campbell, C. T. *J. Phys. Chem. C* **2013**, *117*, 24932−24936.
(104) Joseph, Y.; Kuhrs, C.; Ranke, W.; Ritter, M.; Weiss, W. *Chem. Phys. Lett.* **1999**, *314*, 195−202.

DOI: 10.1021/acscatal.6b01281
ACS Catal. 2016, 6, 4786−4798